REPORT DOCUMENTATION PAGE

1. REPORT DATE (DD-MM-YYYY)	2. REPORT TYPE	3. DATES COVERED (From - To)
21 JUNE 2007	FINAL REPORT	1 AUG 02 - 31 JUL 06

4. TITLE AND SUBTITLE
PHOTOSYNTHETIC PHOTOVOLTAIC CELLS

5a. CONTRACT NUMBER

5b. GRANT NUMBER
F49620-02-1-0399

5c. PROGRAM ELEMENT NUMBER

6. AUTHOR(S)
MARC A. BALDO

5d. PROJECT NUMBER

5e. TASK NUMBER

5f. WORK UNIT NUMBER

7. PERFORMING ORGANIZATION NAME(S) AND ADDRESS(ES)
MASSACHUSETTS INSTITUTE OF TECHNOLOGY
DEPARTMENT OF ELECTRICAL ENGINEERING
77 MASSACHUSETTS AVE, CAMBRIDGE, MA 02139

8. PERFORMING ORGANIZATION REPORT NUMBER

9. SPONSORING/MONITORING AGENCY NAME(S) AND ADDRESS(ES)
AFOSR/NL
875 NORTH RANDOLPH STREET
SUITE 325, ROOM 3112
ARLINGTON, VA 2203-1768
Dr Hugh DeLong

10. SPONSOR/MONITOR'S ACRONYM(S)

11. SPONSOR/MONITOR'S REPORT NUMBER(S)

12. DISTRIBUTION/AVAILABILITY STATEMENT
APPROVE FOR PUBLIC RELEASE, DISTRIBUTION UNLIMITED.

AFRL-SR-AR-TR-07-0199

13. SUPPLEMENTARY NOTES

14. ABSTRACT

Although organic solar cells are a promising source of inexpensive photovoltaic (PV) power, their low efficiency must be improved. We address this problem in a radical departure from the conventional model of organic solar cells. Our architecture is based on photosynthesis - that other example of organic solar cell technology, albeit optimized for two billion years. As in biology, we separate the optical and electrical functions of the solar cell by building an 'antenna' on top of a conventional solar cell. Biomimetic organic solar cells operate as follows: The antenna absorbs the light, and acts to supplement the conventional solar cell - the 'reaction center'. Most importantly, the antenna allows the reaction center to be much thinner, since it no longer must absorb all the light. Thus, its quantum efficiency can approach 100% potentially doubling the performance of organic solar cells.

15. SUBJECT TERMS

16. SECURITY CLASSIFICATION OF:			17. LIMITATION OF ABSTRACT	18. NUMBER OF PAGES	19a. NAME OF RESPONSIBLE PERSON
a. REPORT	b. ABSTRACT	c. THIS PAGE			
					19b. TELEPHONE NUMBER (Include area code)

Photosynthetic photovoltaic cells

M.A. Baldo

MIT, Dept of Electrical Engineering and Computer Science

baldo@mit.edu

Graduate Students

Jon Mapel: (50%) Fabrication and testing of thin film solid state PV structures.
Tim Heidel: (50%) Plasmon-based antennas.
Carlijn Mulder: (50%) Phycobilisome-based solar concentrators
Mike Currie: (50%) Luminescent solar concentrators

Abstract

Although organic solar cells are a promising source of inexpensive photovoltaic (PV) power, their low efficiency must be improved. We address this problem in a radical departure from the conventional model of organic solar cells. Our architecture is based on photosynthesis – that other example of organic solar cell technology, albeit optimized for two billion years. As in biology, we separate the optical and electrical functions of the solar cell by building an 'antenna' on top of a conventional solar cell; see Fig. 1. Biomimetic organic solar cells operate as follows: The antenna absorbs the light, and acts to supplement the conventional solar cell – the 'reaction center'. Most importantly, the antenna allows the reaction center to be much thinner, since it no longer must absorb all the light. Thus, its quantum efficiency can approach 100%, *potentially doubling the performance of organic solar cells*.
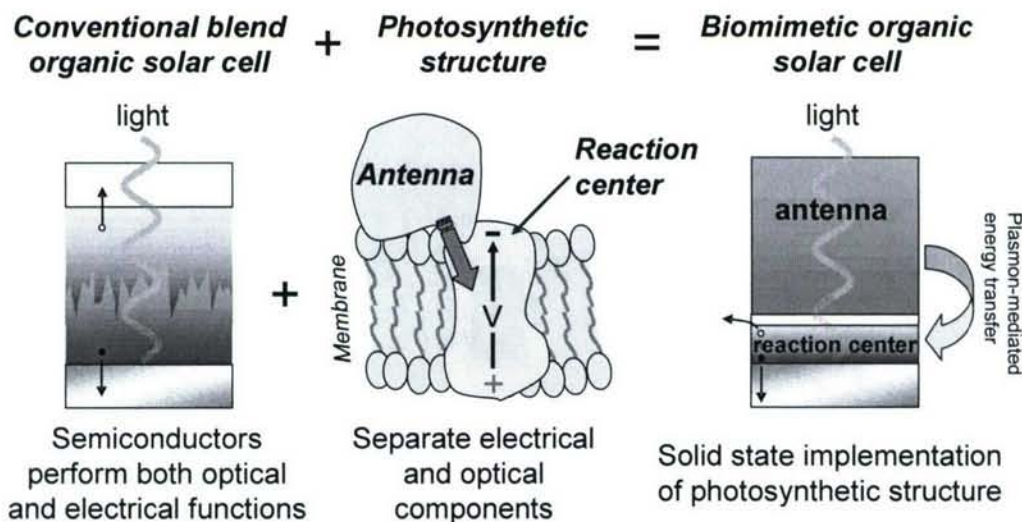
Fig. 1. A comparison between a conventional organic solar cell architecture, photosynthesis, and our external antenna with plasmon-mediated energy transfer. The external antenna allows us to avoid the light absorption/internal quantum efficiency tradeoff common to organic solar cells.

Introduction

The efficiency of solar cells based on molecular materials is presently limited by a fundamental tradeoff:[1]

> *To absorb as many photons as possible, we should employ thick organic semiconducting films. But many of the excitons in thick films are wasted, since they are absorbed too far from a dissociation interface.*

But as shown in Fig. 2, if we could pump thin devices *parallel* to the electrodes, we could achieve much higher absorption efficiencies. Here, we refer to the charge separating structure as a reaction center. It is a conventional PV cell, except it is thinner and optimized for high internal quantum efficiency.
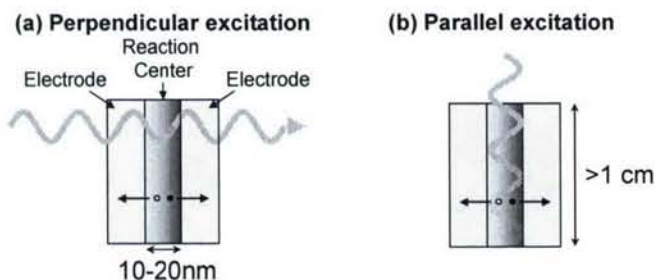

Fig. 2. The geometry of thin-film PV cells. Parallel excitation is most effective, especiallly when the excited states have short diffusion lengths.

Parallel excitation can be achieved by harnessing the guided optical modes of the PV structure. As shown in Fig. 3, we achieve this with an antenna that absorbs incoming photons and then transfers the energy into guided modes: either radiative waveguide modes or non-radiative surface plasmon polariton (SPP) modes.

Fig. 3. Structure of a PV cell with external antenna. There are two processes: (1) The Antenna absorbs incoming photons and then re-emits into surface plasmon polariton modes, and (2) the SPP modes are absorbed by the Reaction Center.
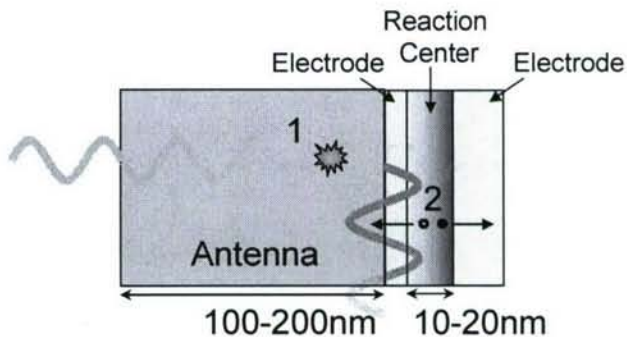
Thus, the biomimetic design splits the electrical and optical functions of solar cells.

Separation of functions allows optimization of the electrical components and optical components independently. For example, we can increase the thickness of the antenna without compromising the electrical performance. Or, we could employ biological materials,[2] such as phycobilisomes, with excellent optical properties but probably poor electrical properties.

This report describes two different approaches to realizing the photosynthetic architecture. In Part 1, we employ surface plasmon polaritons as the guided mode. In Part 2, we use photons.

Part 1. Surface plasmon polariton mediated energy transfer in organic photovoltaic devices

With a theoretical efficiency similar to conventional inorganic photovoltaics (PV) and the potential to be manufactured inexpensively, organic semiconductor technology offers a promising route to ubiquitous solar energy generation. Unfortunately, electronic localization in organic semiconductors yields structured optical absorption spectra with pronounced regions of weak absorption. This limits efficiency because the short exciton diffusion length within organic semiconductors demands uniformly strong absorption.[1]

In this work, we enhance the optical absorption of organic PVs by fabricating a light-absorbing antenna on top of a conventional copper phthalocyanine (CuPC)-based PV; see the device structures in Fig. 4. Light absorbed in the antenna is coupled to the PV, using energy transfer via surface plasmon polaritons (SPPs) and radiation into waveguide modes.[3] SPPs are a particularly effective energy transfer mechanism as they propagate in the plane of the PV rather than parallel to the incident radiation, thereby providing a more efficient means of pumping thin charge generating structures.[4] In addition, the SPP mode extends deeply into both dielectric layers, extending the range of energy transfer up to ~ 100 nm. While this distance is much longer than the range of intermolecular Förster energy transfer, the ~ 100 nm energy transfer limit demands antenna materials with absorption coefficients of at least $\alpha = 10^5$ cm^{-1} to capture sufficient light within the antenna.
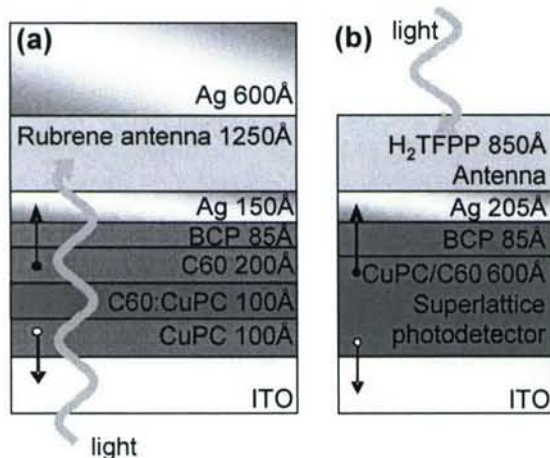

Fig. 4. (a) Devices with resonant antenna cavities have the structure: glass/ indium tin oxide (ITO) (1100 Å)/ copper phthalocyanine (CuPC) (100Å)/ CuPC:fullerene (C60) (1:1) (100Å)/ C60 (200Å) / bathocuproine (BCP) (85Å)/ Ag (150Å)/ 30% Rubrene in CBP antenna (1250Å) / Ag (600Å). To quench or enhance the PL efficiency of the rubrene antenna we introduce either CuPC or DCJTB, respectively, at 2% weight ratio. Concentration quenching is minimized in the antenna by diluting rubrene with CBP. The devices are illuminated from the glass side. Organic materials were purified by vacuum thermal sublimation prior to use. All materials were deposited by thermal evaporation at ~10^{-6} Torr. All active device areas are 0.01 cm^2. (b) For measurement of energy transfer efficiency, high internal quantum efficiency superlattice photodetectors are used with the structure: glass/ ITO (1100Å)/ 20 alternating layers of CuPC and 3,4,9,10-perylenetetracarboxylic bisbenzimidazole (PTCBI) (each layer 15Å)/ BCP(85Å)/ Ag (205Å)/ 5,10,15,20-tetrakis(pentafluorophenyl)porphyrin (H₂TFPP) (850Å). The photoluminescent (PL) efficiency of the H₂TFPP antenna is tuned by adding 4,4'-Bis(N-carbazolyl)-1,1'-biphenyl (CBP) at varying concentrations. The devices are illuminated from the antenna side.

Efficient SPP-mediated energy transfer also requires highly efficient photoluminescent (PL) antenna materials. Unfortunately, the PL efficiency, η_{PL}, of highly absorptive organic semiconductors is typically diminished by intermolecular energy transfer known as concentration quenching. To exploit less absorptive materials with higher η_{PL}, we enclose the antenna within a resonant cavity. As shown in Fig. 4a, the resonant antenna is employed in place of the silver mirror on the back of the cell. Off resonance the antenna acts as a mirror, but near the resonant wavelength the antenna absorption is significantly enhanced, and energy is fed back into the PV cell via SPP-mediated energy transfer. Thus, the resonant antenna structure supplements the performance of the PV cell at resonance, with no degradation off-resonance.

We couple resonant antennas to phthalocyanine-based PV cells, which exhibit a gap in their absorption spectra between the Q and Soret bands. To help fill this gap, we use rubrene, a common organic light emitting device material, which has an absorption coefficient of $\alpha \sim 10^4 \, cm^{-1}$ at $\lambda \sim 550nm$. Using rubrene as a Förster energy transfer donor for the laser dye 4-(dicyanomethylene)-2-t-butyl-6-(1,1,7,7-tetramethyljulolidyl-9-enyl)-4H-pyran (DCJTB), $\eta_{PL} = (90\pm10)\%$.

To tune the resonant antenna PV shown in Fig. 4a, we calculate the expected optical absorption in each layer.[1] A 1250Å-thick film of 30% Rubrene and 2% DCJTB in transparent carbazole biphenyl (CBP) tunes the cavity close to the $\lambda \sim 500$ nm absorption peak of rubrene; see

Fig. **5**. We model energy transfer within a multilayer organic PV stack by evaluating the Poynting vector, **P**, using dyadic Green's functions.[5] The wavevector dependence of energy transfer from the antenna to the PV is shown in Fig. 6a. The energy transfer is plotted against the component of the wavevector parallel to each interface normalized by the wavevector magnitude in the antenna, u. Normalized wavevectors with $u < 1$ correspond to radiative modes while those with $u > 1$ correspond to non-radiative energy transfer. For these calculations, the dipole is located in the middle of the antenna layer. Energy transfer occurs predominantly via non-radiative coupling, mediated by SPP modes with $u > 1$. Loss in the silver layers is significant but is minimized by reducing the thickness of the silver cathode. We also model the dipole coupling efficiency to each layer in the PV stack as a function of the dipole distance from the antenna/cathode interface, see Fig. 6b. Near the cathode, $\eta_{ET} = 54\%$, but the efficiency decreases beyond ~85nm. Averaged over the antenna, $\eta_{ET} = 31\%$.

Fig. 5. Calculated absorption within the resonant cavity device given illumination from glass side. The tuned cavity results in significantly increased absorption in the antenna layer.

4
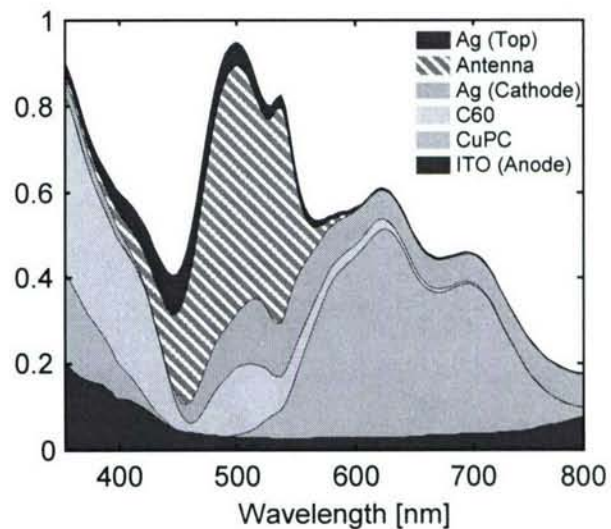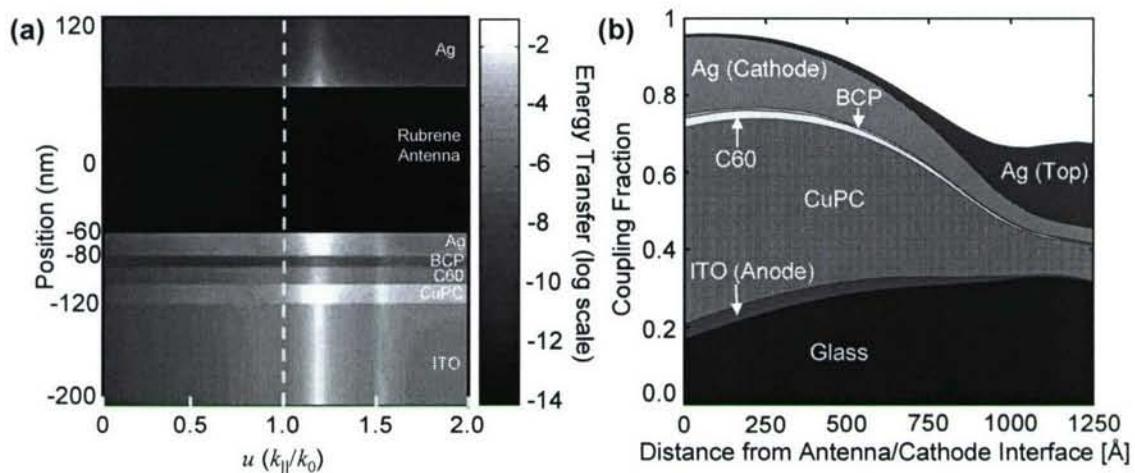
Fig. 6. (a) The normalized in-plane wavevector (u) dependence of energy transfer throughout the resonant cavity devices is shown for dipoles oriented perpendicular to the antenna/cathode interface. The parallel geometry is similar. We assume η_{PL} = 90% at λ = 650 nm. Coupling is greatest for dipoles into modes with $u>1$, corresponding to surface plasmon polaritons (SPPs). **(b)** The modeled dipole coupling fraction to each layer in the photovoltaic stack as a function of the dipole distance from the antenna/cathode interface. Coupling to the CuPC and C60 layers results in photocurrent.

To demonstrate the potential improvement possible using an external resonant antenna in conventional C60/CuPC PV cells, we compare the rubrene/DCJTB antenna device to a control device without the antenna. Quenched antennas were also fabricated with the addition of 2% of the quenching material CuPC instead of DCJTB. External quantum efficiency measurements were made using a xenon lamp with monochromator, chopped at f = 90 Hz, and measured using a lock-in amplifier. Light intensity was measured with a calibrated silicon photodiode. The external quantum efficiencies of these devices as a function of wavelength are shown in Fig. 7 and compared to the reflectivity of the antenna cavity. The absorption of the antenna (from

Fig. **5**) and the internal quantum efficiency at the PL maximum of DCJTB, η_{IQE} = (30±10)% at λ = 640nm, is used to determine η_{ET}. This yields η_{ET} = (25±10)%, consistent with the calculated result of η_{ET} = 31% in Fig. 3b. As illustrated, with improved energy transfer, the efficiency in the spectral gap between absorption peaks could be significantly improved. The absorption modeling also demonstrates that the improved quantum efficiency outside the region where the resonant cavity absorbs is due to reflectivity changes that modify the electric field profile within the device.

While the introduction of the antenna necessarily adds a step into the energy transduction process, it can be successfully employed in spectral regions where the absorption fraction of the PV cell drops below η_{ET}. To reduce the uncertainties in the measurement of η_{ET}, we fabricate an organic superlattice photodetector and antenna without the resonant cavity; see Fig. 4b. This structure should also enhance η_{ET}, since it allows thicker CuPC layers while maintaining a high η_{IQE}, thereby increasing the absorption of SPPs in the charge generating layers.
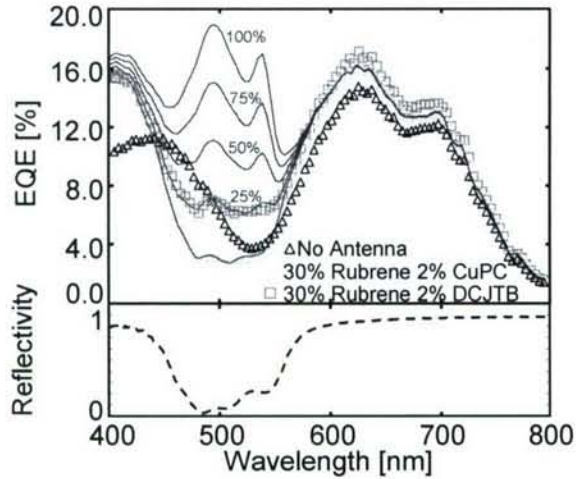
Fig. 7. External quantum efficiency (EQE) for resonant antenna devices. Devices with functional external rubrene-based antenna layers exhibit an increase in EQE over the wavelength range where rubrene absorption occurs and the cavity reflectivity decreases. Functional antennas (□) employ the laser dye, DCJTB, whereas nonfunctional antennas ( ) employ the quencher CuPC. The functional antenna shows a significant performance enhancement versus both the quenched antenna and devices fabricated without any antenna (Δ). Comparison with modeling (—) indicates that the energy transfer efficiency is approximately 25%. We also show the expected EQE for energy transfer efficiencies of 0%, 50%, and 75%.

Under an applied bias, the organic superlattice photodetector is expected to exhibit an internal quantum efficiency close to 100% for excitation by SPP-modes.[4,6] We assume $\eta_{IQE} = 100\%$ which gives a lower bound for η_{ET}. The antenna material in this device is tetrakis(pentafluorophenyl)porphyrin (H$_2$TFPP). It is chosen for its combination of moderate PL efficiency ($\eta_{PL} = 2\text{-}3\%$) and high absorption coefficient ($\alpha = 10^6$ cm^{-1} at $\lambda = 400$nm) that allows nearly 100% of incident radiation to be absorbed in the absence of a cavity within the ~100 nm range of SPP-mediated energy transfer.

External quantum efficiency measurements were made at a reverse bias of 3.5V. The *measured* absorption and PL efficiency of the H$_2$TFPP antenna is used to determine η_{ET} from the increase in external quantum efficiency, $\Delta\eta_{EOE}$, i.e. $\eta_{ET} = \Delta\eta_{EOE}/\eta_{ABS}/\eta_{PL}$. Four H$_2$TFPP antennas were fabricated with varying PL efficiencies by blending H$_2$TFPP with different concentrations of CBP. The addition of CBP reduces concentration quenching. To eliminate energy transfer altogether, additional devices were fabricated with non-functional antennas comprised of H$_2$TFPP codeposited with 3.5% of CuPC. Using the quenched antenna as the baseline, and noting that the absorption of H$_2$FTPP is $\eta_{ABS} = 75\%$ for $\lambda \leq 450$ nm, we obtain $\eta_{ET} = (51\pm10)\%$, substantially higher than the resonant antenna result; see the inset of Fig. 8. Note that the overall change in quantum efficiency is lower, however, due to the weak η_{PL} of H$_2$TFPP.

The peak efficiency of SPP-mediated energy transfer in previous studies[3] was approximately $\eta_{ET} = 5\%$[5], too small for most applications. The approximately order of magnitude improvement in this work is due to reductions in the thickness of the interfacial silver layer, and increasing SPP absorption in the organic semiconductors, which must compete with SPP loss in the silver layer. It is possible to increase the quantum efficiency of an antenna further by optimizing the orientation and position of luminescent antenna excitons with respect to the thin Ag cathode.

6
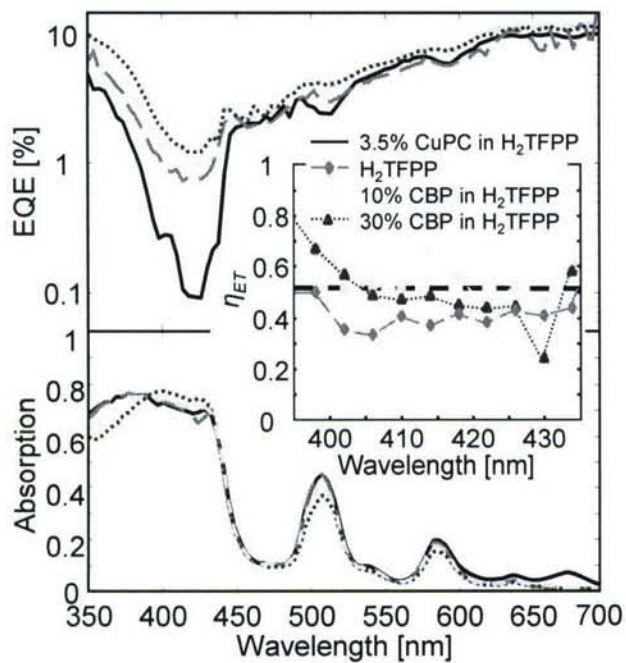
Fig. 8. Measurement of energy transfer efficiency using superlattice photodetectors. Top: Measurement of external quantum efficiency of devices with different antenna compositions: 3.5% CuPC in H_2TFPP $\eta_{PL} = 0\%$ (solid), 100% H_2TFPP $\eta_{PL} = (2.4\pm0.2)\%$ (long dashed), 90:10 H_2TFPP:CBP $\eta_{PL} = (2.5\pm0.3)\%$ (short dashed), 70:30 H_2TFPP:CBP $\eta_{PL} = (3.4\pm0.3)\%$ (dotted). Bottom: absorption spectra of different antenna layers on glass. Inset: Calculation of energy transfer efficiency normalized by the PL efficiencies of the various antennas yields $\eta_{ET} = (51\pm10)\%$.

7

Part 2. High Efficiency Luminescent Solar Concentrators

The aim: Reducing the cost of photovoltaic energy

Photovoltaic (PV) cells remain expensive relative to alternative sources of electrical power. Their cost is measured per Watt of peak power generated: $\$/W_p$. It is a function of the manufacturing cost per unit area of the PV, divided by the power conversion efficiency:

$$\$/W_p = \frac{\text{PV cost}}{\eta_p} \tag{1}$$

This work addresses the cost of PV cells. The industry standard is probably First Solar Inc. Their current manufacturing cost for CdTe-based cells is approximately $\$1.50/W_p$.[7] First Solar's semiconductor and semiconductor-related capital costs are estimated to be only $\$0.08/W_p$, or approximately 10% of their total materials costs.[8] Despite this remarkable achievement, their overall cost of $\$1.50/W_p$ is still significantly more expensive than the US Department of Energy's goal of $\$0.33/W_p$.

The First Solar example demonstrates that PV costs below $\$1/W_p$ cannot be obtained merely by employing inexpensive semiconductors. Rather, the fundamental structure of PV cells must be simplified.

Solar Concentrators

In this report we seek to lower the cost of PV energy by utilizing solar cells more efficiently.

Conventional solar cells use large areas of expensive crystalline Si or GaAs to collect light. But this is an inefficient use of high quality semiconductor materials. Organic dyes, for example, are cheaper and more absorptive; see Fig. 9. The benefit of crystalline semiconductors is their high quantum efficiency of charge separation and charge extraction; electrical properties that are difficult to obtain inexpensively because they originate in purity and crystalline order.

	Copper phthalocyanine	Si
Abs. coefficient	10^5 cm^{-1}	10^4 cm^{-1}
Annual production	~ 75 kilotons	~ 35 kilotons
Cost in PVs	$0.17/m^2	> $10/m^2

Fig. 9. A comparison of the common dye molecule copper phthalocyanine (CuPC) and crystalline Si. CuPC is more absorptive, cheaper, and produced in greater quantities.

Concentrators separate the functions of light collection and charge generation. In a concentrator light is gathered by a large, inexpensive collector. The collected light is focused on a small area of high performance semiconductor such as crystalline Si or GaAs. The ratio of the area of the collector to the area of the PV cell is known as the geometric factor, G. The attraction of the concentrator approach is that the complexity of a large area solar cell is replaced by a simple optical collector. PV cells are still required, but large G values can render their cost negligible, potentially lowering the overall $\$/W_p$. Thus, the cost model for a solar concentrator is a function

8

of the manufacturing cost per unit area of the PV and the collector cost per unit area, as well as η_p and G:

$$\$/W_p = \frac{\text{collector cost}}{\eta_p} + \frac{\text{PV cost}}{G\eta_p} \qquad (2)$$

Thus, the design of a solar concentrator requires: (*i*) minimizing the collector cost, (*ii*) maximizing η_p (to defray the collector cost) and (*iii*) maximizing $G\eta_p$ (to defray the PV cost).

We will not address the manufacturing cost of the collector or the PV. These parameters are influenced by economies of scale. Rather, we seek to determine the feasibility of the technology. We seek to maximize η_p and $G\eta_p$ in *luminescent* solar concentrators.

Luminescent Solar Concentrators

Conventional light concentration uses mirrors to focus light onto a solar cell. For optimum performance, the focal point of the light must be maintained as the sun transits the sky. The concentrator requires mechanical tracking to maintain the focal point. Such systems are expensive to maintain and deploy. They also require extra spacing to avoid shadowing neighboring concentrators. The simplicity of the flat solar panel is lost.

First proposed in the 1970's,[9-11] luminescent solar concentrators (LSCs) consist of a transparent waveguide, such as a sheet of glass, doped with a dye. Light incident on the waveguide is absorbed by the dye and then re-emitted into a guided mode that propagates until it is absorbed by a PV cell.
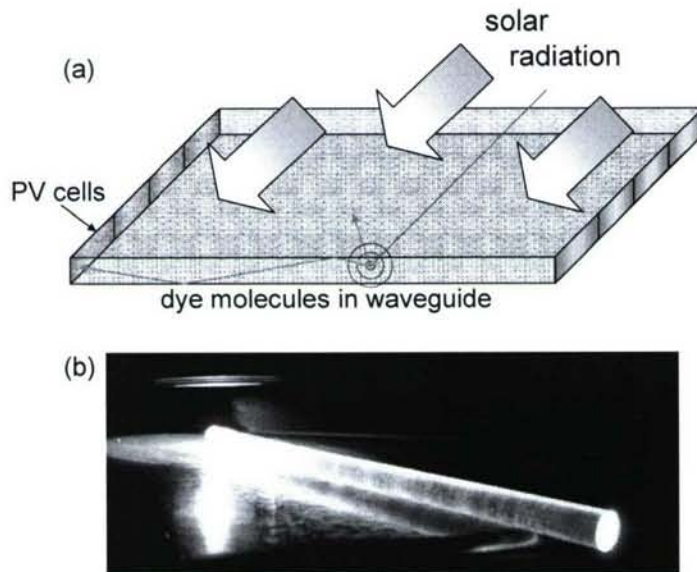

Fig. 10. **(a)** A luminescent solar concentrator. Incident light is absorbed and re-radiated by dyes within a transparent waveguide. **(b)** The operation of an LSC is demonstrated by illuminating one end of a dye doped polymer rod.

Assuming photons are emitted isotropically by the dye, the solid angle trapped by total internal reflection is

$$\Omega = 2\pi \int_{-\sin^{-1} n_{clad}/n_{core}}^{\sin^{-1} n_{clad}/n_{core}} d\theta \sin\theta \tag{3}$$

Normalizing by the full 4π solid angle gives the trapping efficiency, η_{trap}

$$\eta_{trap} = \sqrt{1 - \frac{n_{clad}^2}{n_{core}^2}} \tag{4}$$

For a simple glass waveguide, with core and cladding refractive indices of $n_{core} = 1.5$ and $n_{clad} = 1$, respectively, approximately 75% of the re-emitted photons will be trapped.

Larger trapping efficiencies are also possible. Later in the report we will describe LSCs constructed with $n_{core} = 1.7$ and $\eta_{trap} = 81\%$. It is also possible to employ an omnidirectional reflector to ensure that $\eta_{trap} = 100\%$; see Specific Aim #3.

The Thermodynamic Limits of Luminescent Solar Concentrators

The concentration limit for diffuse incoming radiation is n^2, where n is the refractive index of the concentrator. For example, Fresnel lens concentrators typically achieve concentrations of a factor of two. In contrast, luminescent solar concentrators behave like optical heat pumps.[12] Light is absorbed at one energy and re-emitted at a lower energy.[12] The energy difference is lost to heat, but this allows the radiance at the lower energy to be increased far beyond the n^2 limit.[12] The maximum power efficiency is determined by the absorption cutoff of the dye; see Fig. 11.
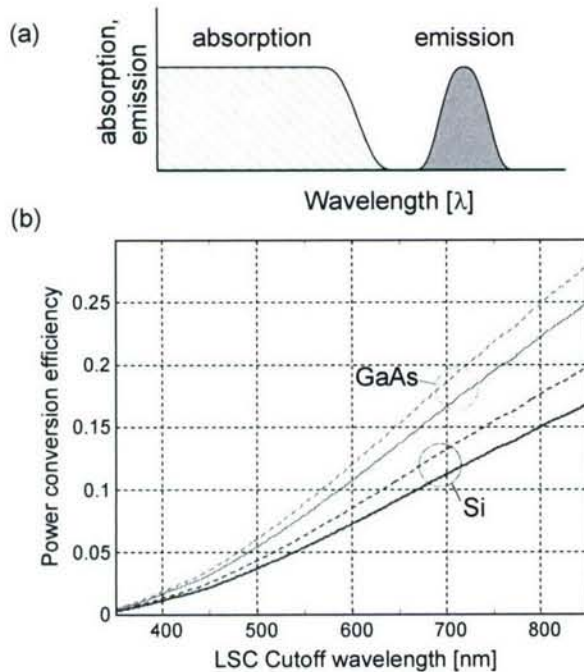
Fig. 11. A calculation of the maximum performance of an LSC that absorbs all solar radiation below a cutoff wavelength. For an LSC coupled to Si PV cells, we have assumed $V_{OC} = 0.68V$, $FF = 0.801$. These results are typical of high quality Sunpower cells. For the GaAs cells, we have assumed $V_{OC} = 1.01V$, $FF = 0.8$. Dotted lines are estimates of the improvement in V_{OC} for 100 x concentration of solar flux. Given a restriction to dyes operating in the visible or near IR, GaAs is clearly the preferred match.

10

The maximum concentration factor for a given dye is determined from thermodynamic arguments:[12]

$$G \approx \frac{\varepsilon_2^2}{\varepsilon_1^2} \exp\left[\frac{\varepsilon_1 - \varepsilon_2}{kT}\right]. \tag{5}$$

Here, ε_1 and ε_2 are the energies of the absorption cutoff and emission, respectively. For a dye with absorption cutoff at $\lambda = 650$nm, and emission peaked at $\lambda = 770$nm, $G = 10^5$.

The emission wavelength in a LSC is ideally placed just below the absorption cutoff of the PV cell. Thus, the wavelength shift between the dye's absorption and emission reduces the spectral range of the PV cell. But it is important to note that solar radiation in the gap between absorption and emission is not necessarily wasted. It is transmitted through the collector and can be gathered by another collector or used to heat water in a hybrid photovoltaic thermal system.
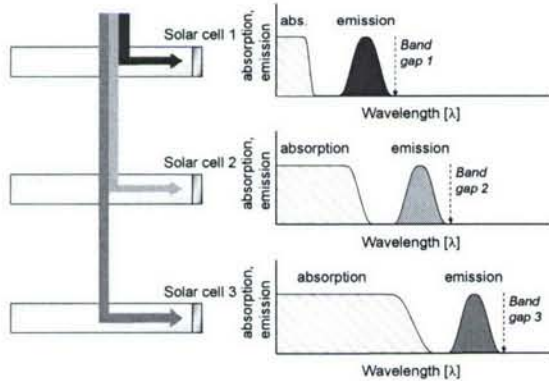
Fig. 12. The LSC equivalent of a multiple junction solar cell. In principle the approach can be extended well above the theoretical single junction limit. After Barnham, et al.[13]

The Advantages of LSCs

(i) *Simple construction using low cost materials*
LSCs are simpler than PV cells. The only components are the waveguide, the dyes and a package. No conductive electrodes are required across the collector area. The transparent conductive electrode is expected to be the most expensive component in thin film PV cells.[14] The collector also does not require scare materials such as In, Ge or Te.

(ii) *High power efficiencies are possible*
As shown in Fig. 11 the power efficiency, η_p, of a luminescent can approach that of a high performance crystalline PV cell.

(iii) *Large Concentration Factors*
Since only the edges of the waveguide are covered by PV cells, the concentration factor, G, is the ratio of the window width to thickness, divided by the number of edges covered by solar cells. In our preliminary results we will demonstrate efficient concentrators with $G > 25$, but the theoretical limit is much larger; see Eq. (5). It may be possible to exceed $G = 1000$.

(iv) *Improved open circuit voltage*
Concentration improves the open circuit voltage of traditional solar cells by approximately 60 mV per decade of solar flux. This can be significant for $G > 10$.

11

(v) *Minimal heating*

Traditional mirror-based concentrators usually require cooled PV cells. But cooling is not required in LSCs because heat is dissipated across the collector rather than in the PV cells. Photons with energies above the PV's bandgap are downshifted in the absorbing dye molecules rather than in the PV. In addition, sub-gap infrared radiation is not focused on the PV cell as in a conventional mirror-based concentrator. Rather it is transmitted through the collector. If desired the infrared radiation can be used to supplement the performance of the LSC by heating water.

(vi) *No tracking required*

The dye molecules are randomly oriented hence the capacity factor is optimal.

(vii) *Defect tolerant*

LSCs are intrinsically tolerant of defects because of the many parallel paths available to re-emitted photons to the encircling PV cells. In contrast, short or open circuit failures in PV arrays can be damaging.

Obstacles to LSCs

Despite these potential benefits, early work on LSCs failed to overcome two crucial obstacles: *self absorption* and *photostability*. Consequently, only a bare minimum of work on LSCs has persisted since the early 1980's.

(i) Photostability

The key stability concern in LSCs is the emissive dye. This dye is typically a red or infrared emitter. Since work on LSCs was largely abandoned there have been significant investments in the research and development of organic light emitting devices (OLEDs). This work has resulted in red OLEDs that now routinely exhibit half-lives exceeding 300,000 hours, or thirty years. Progress in OLED stability was achieved by advances in dye molecule design and packaging. Both of these technologies are directly applicable to LSCs.

(a)

Glass or steel can   dessicant

Epoxy or other sealant   OLED

(b)

	η_Q	η_{PL}^{*}	Lifetime to 50%
blue	11%	46%	17,500 hrs @ 200 cd/m²
green	17% 10%	71% 42%	25,000 hrs @ 1000 cd/m² 40,000 hrs @ 1000 cd/m²
red	19%	80%	300,000 hrs @ 500 cd/m²
deep red	19%	80%	200,000 hrs @ 500 cd/m²
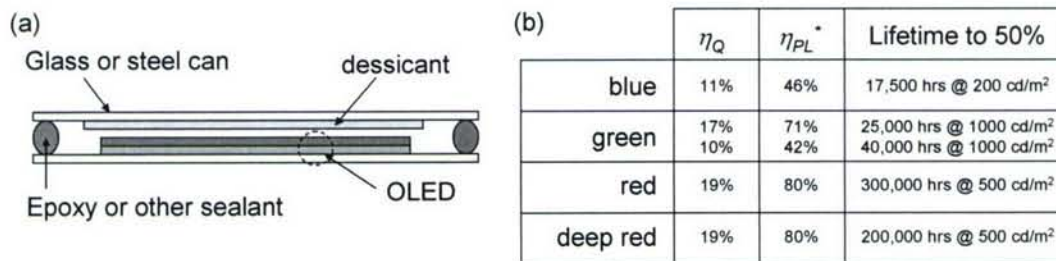
Fig. 13. **(a)** OLED packaging technology is directly relevant to LSCs. **(b)** In recent years the operational stability of OLEDs has exceeded 30 years. Here we show stability data from Universal Display Corporation's set of phosphorescent dye molecules. We also plot the external quantum efficiency of the OLEDs and an estimate for the *minimum* photoluminescent efficiency of each dye calculated by assuming a maximum of 24% outcoupling.[5] Excitation densities within OLEDs are significantly higher than expected in LSCs. Nevertheless the OLED example proves that the photostability problem can be solved (especially in the red and near IR, where it matters most for LSCs).

12

(ii) Self Absorption in LSCs

It is essential that the dye in a LSC be transparent to its own radiation, otherwise re-radiated light will be rapidly re-absorbed. If it is reabsorbed, there are two potential loss processes: the photoluminescent efficiency, η_{PL}, may be less than unity and the energy may non-radiatively decay to heat; or the waveguide trapping, η_{trap}, may be less than unity and the photon may be re-emitted outside the guide.

air

glass

air
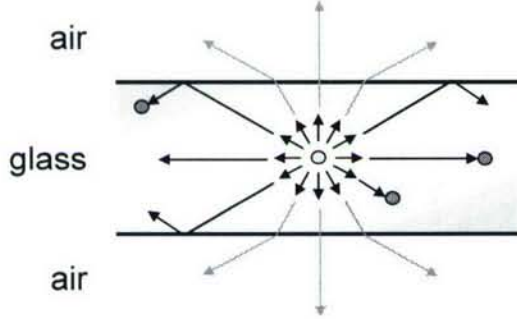
Fig. 14. Radiation from a dye molecule may leave the waveguide or be absorbed by other dye molecules. Such self absorption is an important source of loss.

Let's define r to be the self absorption probability for a photon in the waveguide. It is a function of the overlap between the normalized emission spectrum of the dye $f(\lambda)$ and the absorption coefficient of the dye $\alpha(\lambda)$. The absorption coefficient must be scaled by the concentration of the dye within the waveguide. We express the concentration as the effective thickness of the dye layer, t, divided by the thickness of the waveguide, D. For a dye molecule in the center of a square LSC with length L, the self absorption is given by

$$r = \frac{\int_0^\infty d\lambda \int_{\theta_{crit}}^{\pi/2} \sin\theta d\theta \int_{-\pi/4}^{\pi/4} d\phi f(\lambda)\left(1 - \exp\left[-2\alpha(\lambda)tG/\sin\theta\cos\phi\right]\right)}{\int_0^\infty d\lambda \int_{\theta_{crit}}^{\pi/2} \sin\theta d\theta \int_{-\pi/4}^{\pi/4} d\phi f(\lambda)} \tag{6}$$

where we noted that the geometric factor is $G = L/4D$. We can simplify this expression in the case of weak self absorption

$$r \approx 2G\frac{1 - 2\theta_{crit}/\pi}{\cos\theta_{crit}}\log\left(3 + 2\sqrt{2}\right)\int_0^\infty d\lambda f(\lambda)\alpha(\lambda)t \tag{7}$$

Note that the self absorption increases linearly with the geometric factor. Once a photon is reabsorbed it may be re-emitted and eventually reach the PV. The net contribution of multiple reabsorption events is described by a geometric series. Thus, the internal quantum efficiency, η_{IQE}, defined as the fraction of absorbed photons that are guided to the PV, is:

$$\eta_{IQE} = \eta_{PL}\eta_{trap}(1-r) + \eta_{PL}\eta_{trap}r\eta_{PL}\eta_{trap}(1-r) + \eta_{PL}\eta_{trap}r^2\eta_{PL}^2\eta_{trap}^2(1-r) + ... \tag{8}$$

Simplifying Eq. (8) yields

$$\eta_{IQE} = \frac{\eta_{PL}\eta_{trap}(1-r)}{1-r\eta_{PL}\eta_{trap}}$$

(9)

This expression is plotted in Fig. 15.
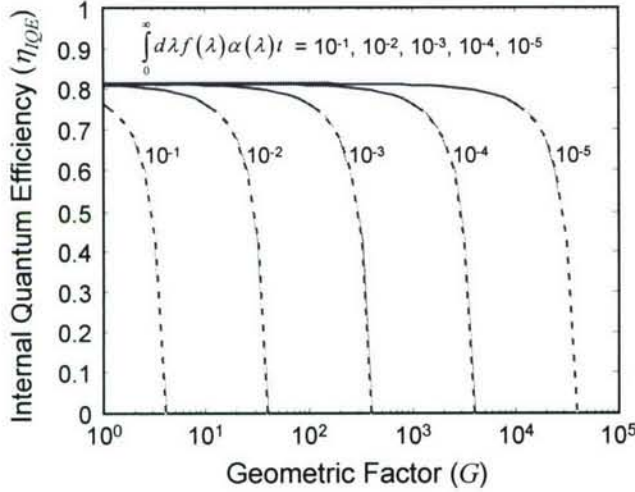
Fig. 15. The internal quantum efficiency as a function of the concentration factor. We have assumed $\eta_{trap} = 81\%$ and $\eta_{PL} = 100\%$. The efficiency is plotted for various absorption-emission overlap integrals. Dotted lines indicate that the result is inaccurate since the self absorption probability is too large for the assumption leading to Eq. (7).

The rule of thumb is that to achieve a desired geometric concentration factor, G, we require

$$G < \left(10\int_0^\infty d\lambda f(\lambda)\alpha(\lambda)t\right)^{-1}$$

(10)

While the Stokes shift between absorption and emission renders most organic dyes quite transparent to their own fluorescence, the self absorption requirements of LSCs are extremely stringent. The ratio of self absorption to the dye's peak absorption must be on the order of the concentration factor. For example, consider a 2mm-thick waveguide that is 1m wide. The concentration factor is 500. Thus, the self-absorption must be less than 1/5000th of the peak absorption of the dye. This is difficult to achieve with traditional laser dyes. For example, the classic laser dye DCM, which was preferred by Zewail, *et al.*[9,10] in their pioneering 1979 study has a normalized self absorption of approximately 10%, which limits the concentration factor to $G \sim 1$.

(iii) Power efficiency

To date, the best combination of LSC performance ($\eta_P = 2\%$, and $G\eta_P = 50\%$) was achieved using DCM.[9,10] As we have demonstrated, these results are *significantly* below the theoretical limits of an LSC. Furthermore, it is striking that the DCM result has not been bettered since the original 1979 study. These low η_P and $G\eta_P$ results are the most important obstacle to LSCs.

Research Aim:
Exploiting Förster Energy Transfer for Improved $G\eta_P$

Near field energy transfer can be used to enhance the wavelength shift between self absorption and emission. In particular, Förster energy transfer, which couples the transition dipoles of neighboring molecules, can be exploited to couple a dye with short wavelength absorption to a dye with longer wavelength absorption.
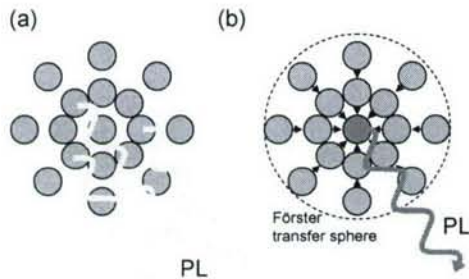

Fig. 16. (a) In a pure film absorption and emission of light is performed by the same molecular species. (b) When a second, lower energy, dye is added, the host material can transfer energy to it *without emission of a photon*, introducing a substantial energy shift between absorption and emission.

We implemented Förster energy transfer to improve the performance of Zewail et al's DCM-based concentrator. In the new low-self absorption concentrator, DCM is employed in much lower concentrations. Optical absorption is instead performed by two common OLED materials, tris(8-hydroxyquinoline) aluminum (AlQ_3) and rubrene. Both materials are fluorescent at high concentrations and are therefore capable of energy transfer to a low density of DCM. Because Förster energy transfer is a short range (~3-4nm) interaction, all the dyes are co-evaporated in a thin film. The substrate is a $10\times10\times0.1$ cm glass sheet with $n_{core} = 1.7$ and a Sunpower Si-based solar cell attached to one edge. Earlier concentrators were made by diffusing dyes within a polymer substrate.[9,10] However, the low dye density in such devices precludes the use of Förster transfer to minimize self absorption.

The absorption and emission spectra of the pure DCM and the modified concentrators are shown in Fig. 17. Note that in these devices DCM has been replaced by a modern variant DCJTB.
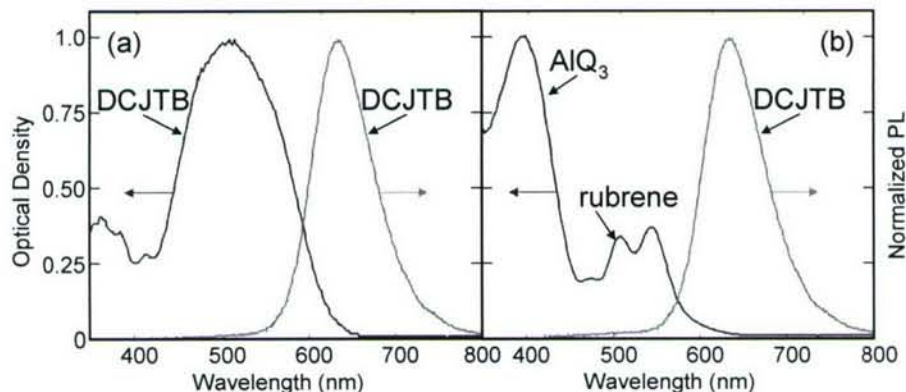
Fig. 17. (a) The absorption spectrum of DCJTB shows significant overlap with its emission spectrum. (b) At lower concentrations of DCJTB the self absorption is reduced. Here, photons are absorbed by AlQ_3 and rubrene.

15

The external quantum efficiency of an AlQ$_3$/rubrene/1% DCJTB device with $G = 25$ is shown in Fig. 18.
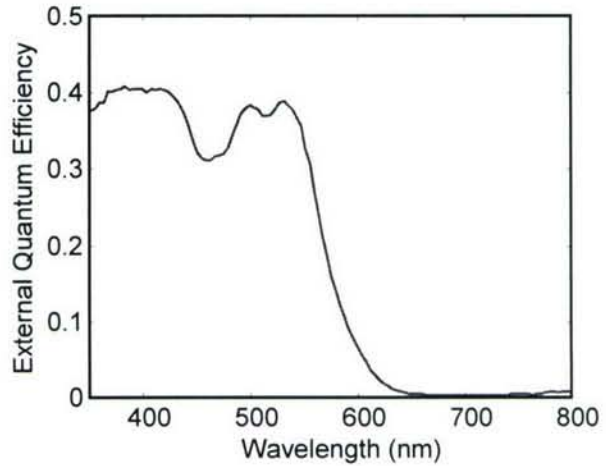
Fig. 18. The external quantum efficiency of the 1% DCJTB concentrator as recorded in the center of the glass substrate.

We also plot the quantum and power efficiencies in Fig. 19.
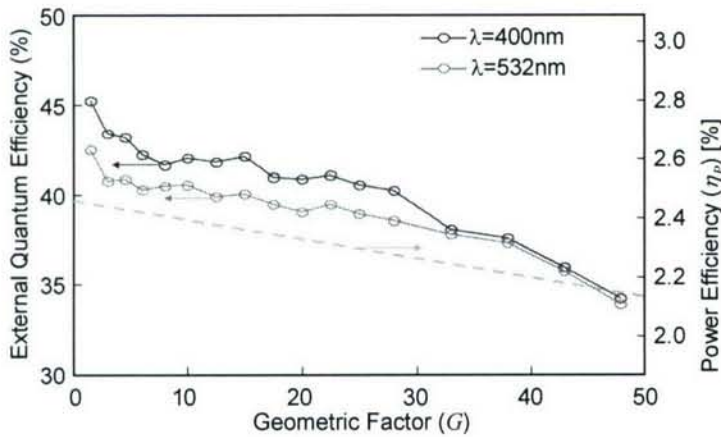
Fig. 19. The external quantum efficiency and power efficiency of the 1% DCJTB concentrator decrease linearly as expected from Eqs. (7) and (9).

Similar to the original[9,10] DCM-based concentrator, the power efficiency in this device is $\eta_P = 2.3\%$ (for $G = 25$). But the lower self absorption is of benefit at high geometric factors when $G\eta_P \sim 100\%$, approximately twice the performance of previous results.

The ideal dye complex of Fig. 16 looks very similar to a phycobilisome. Hence our current work aims to implement LSCs using phycobilisomes. We are building glass wells for phycobilisomes in solution and attaching a solar cell to one edge.

Summary of outcomes this year

Publications

1. Novel energy transfer
- Our energy transfer theory was published in Optics Express[5]

2. Krestchmann measurements of SPP losses in organic PV cells.
- This was published in Applied Physics Letters[4]

3. SPP-mediated resonant antennas
- This is currently in review.

4. Luminescent solar concentrators
- We are writing this up and considering commercialization of the technology.

5. Phycobilisome-based solar concentrators
We are preparing this work as a follow-on to the LSC paper.

Patents

We have filed for two patents:
1. Photovoltaic cells with external antennas
2. Luminescent solar concentrators

References

1. Peumans, P., Yakimov, A. & Forrest, S. R. Small molecular weight organic thin-film photodetectors and solar cells. *Journal of Applied Physics* **93**, 3693-3723 (2003).
2. Das, R., Kiley, P. J., Segal, M., Norville, J., Yu, A. A., Wang, L., Trammell, S., Reddick, L. E., Kumar, R., Zhang, S., Stellacci, F., Lebedev, N., Schnur, J., Bruce, B. D. & Baldo, M. Solid State Integration of Photosynthetic Protein Molecular Complexes. *Nano Letters* **4**, 1079-1083 (2004).
3. Andrew, P. & Barnes, W. L. Energy transfer across a metal film mediated by surface plasmon polaritons. *Science* **306**, 1002-1005 (2004).
4. Mapel, J. K., Singh, M., Baldo, M. A. & Celebi, K. Plasmonic excitation of organic double heterostructure solar cells. *Applied Physics Letters* **90** (2007).
5. Celebi, K., Heidel, T. D. & Baldo, M. A. Simplified calculation of dipole energy transport in a multilayer stack using dyadic Green's functions. *Optics Express* **15**, 1762-1772 (2007).
6. Peumans, P., Bulovic, V. & Forrest, S. R. Efficient, high-bandwidth organic multilayer photodetectors. *Applied Physics Letters* **76**, 3855-3857 (2000).
7. First Solar, Inc. Amendment No. 8 to Form S-1 filed with the Securities and Exchange Commission on November 15th 2006.
8. Zweibel, K. Issues in thin film PV manufacturing cost reduction. *Solar Energy Materials and Solar Cells* **59**, 1-18 (1999).
9. Batchelder, J. S., Zewail, A. H. & Cole, T. Luminescent Solar Concentrators .1. Theory of Operation and Techniques for Performance Evaluation. *Applied Optics* **18**, 3090-3110 (1979).
10. Batchelder, J. S., Zewail, A. H. & Cole, T. Luminescent Solar Concentrators .2. Experimental and Theoretical-Analysis of Their Possible Efficiencies. *Applied Optics* **20**, 3733-3754 (1981).
11. Yablonovitch, E. Thermodynamics of the Fluorescent Planar Concentrator. *Journal of the Optical Society of America* **70**, 1362-1363 (1980).
12. Smestad, G., Ries, H., Winston, R. & Yablonovitch, E. The thermodynamic limits of light concentrators. *Solar Energy Materials* **21**, 99-111 (1990).
13. Barnham, K., Marques, J. L., Hassard, J. & O'Brien, P. Quantum-dot concentrator and thermodynamic model for the global redshift. *Applied Physics Letters* **76**, 1197-1199 (2000).
14. Zweibel, K. Thin film PV manufacturing: Materials costs and their optimization. *Solar Energy Materials and Solar Cells* **63**, 375-386 (2000).

New Bio-Inorganic Photo-Electronic Devices Based on Photosynthetic Proteins

Nikolai Lebedev

US Naval Research Laboratory, 4555 Overlook Ave., Washington, DC 20375

University of Virginia, Gilmer Hall, Charlottesville, VA 22904

ABSTRACT

The photosynthetic reaction center (RC) is one of the most advanced light sensing and energy converting materials developed by Nature. Its coupling with inorganic surfaces is attractive for the identification of the mechanisms of interprotein electron transfer (ET) and for the possible applications for the construction of protein-based innovative photoelectronic and photovoltaic devices. Using genetically engineered bacterial RC proteins and specifically synthesized organic linkers, we were able to construct self-assembled and aligned biomolecular surfaces on various electrodes, including gold, carbon, indium tin oxide (ITO), highly ordered pyrrolytic graphite (HOPG) and carbon nanotube (CNT) arrays. Our results show that, after immobilization on the electrodes, the photosynthetic RC can operate as a highly efficient photosensor, optical switch, and photovoltaic device.

bioelectronics, biophotonics, self-assembly, photosynthetic reaction center, photovoltaic, interface

1. INTRODUCTION

The development of the next generation of nature inspired highly efficient energy converting devices, sensors, or information processing devices requires integration of biological and inorganic materials, and ultimately will lead to the construction of integrated bio-inorganic hybrids [1, 2]. The advantages of photosynthetic proteins for use in photo-energetic and photo-electronic devices include their extremely high efficiency, ultra-low size and weight, precise and highly reproducible spatial organization, the possibility of heatless amplification and processing of electronic signal, the relative simplicity of construction and modification, and the possibility of device self assembly, self healing, and adaptation [2, 3]. The main problem in the construction of such devices is overcoming the energy barrier between biomolecules and the electrode, allowing for efficient charge separation and electron transfer [4].

The high efficiency of primary charge separation in photosynthetic RCs is due to directed vectorial electron transfer (ET) within the protein which leads to the formation of a dipole with the field density of about 10^6 V/cm (Fig. 1) [5]. This dipole has a life time about 0.1 s that is several orders of magnitude longer than the time of its formation (0.2 ns) [2, 6-8]. To exploit the advantages of RC and to generate an electric current from the RC dipole, the protein must be properly bound and oriented to the electrode. In principle, the protein can be bound to the electrode through either its primary donor (P-side) or acceptor side (Q-side, or H-subunit) (Fig. 1B) [9]. Recently we initiated a series of experiments studying the possibility of using the RC protein in construction of photoelectronic and photovoltaic devices. We constructed protein monolayers on the surfaces of carbon and gold electrodes with the RC attached to the electrode by either its P-or Q-sides [4, 10]. Then we tested the functional activity of the constructed devices and their dependence on the protein orientation, distance to electrode, bias voltage, and the type of protein binding (wiring) to the electrode.

2. VECTORIAL PHOTO-INDUCED ELECTRON TRANSFER BETWEEN ELECTRODE AND PHOTOSYNTHETIC PROTEINS

In our experiments we used genetically engineered RC proteins from *R. sphaeroides* containing a polyhistidine tag at the C-terminal end of M subunit at close proximity to the RC primary donor, P (Fig. 1) [4, 10]. The protein was expressed in SMpHis strain of *R. sphaeroides* and purified on a Ni–nitrilotriacetic acid (Ni–NTA) column as described elsewhere [4, 11, 12]. For unidirectional binding of the protein to electrode through the tag, we constructed a bifunctional linker with one end having an NTA group to be attached to the protein and the other end having a pyrene group to be

attach to carbon electrode or thiol group to be attached to gold or indium tin oxide (ITO). For the construction of protein monolayers with the alternative RC orientation we used N-(1-pyrene)iodoacetamide that binds photosynthetic RC to the electrode through a single Cys group exposed at the surface of H subunit [13]. Two surfaces with opposite protein orientations allows us to compare the efficiency of the ET between the protein and the electrode at protein orientation with donor (P-side) or acceptor (H-subunit side) facing the electrode. In some experiments we utilize a carbon coated gold grid as the electrode. The high conductivity of the carbon film allows the grid to function as an efficient electrode [14, 15] and this same substrate permits the direct observation of the RC films by transmission electron microscopy.
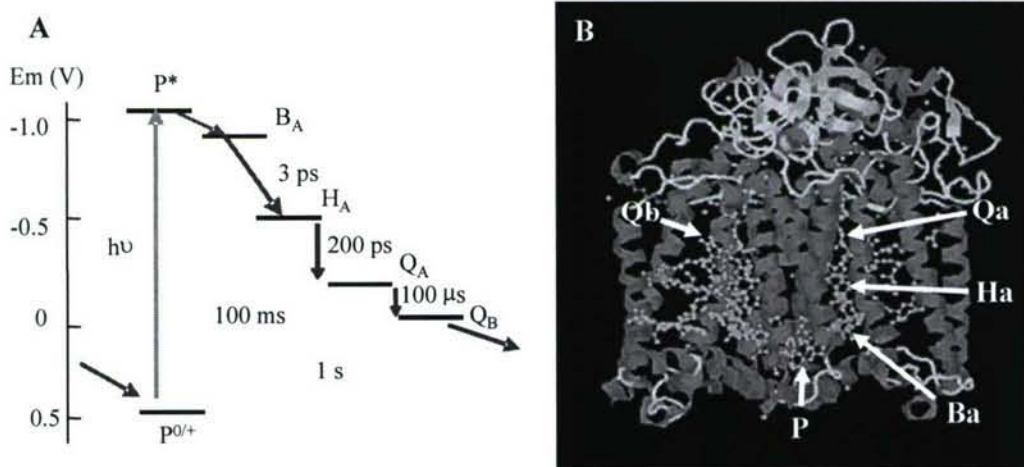

Fig. 1. A. Energy and kinetic diagram of electron-transfer in photosynthetic RC of *R.capsulatus*. P, B, H and Q denote bacteriochlorophyll special pair (primary donor), monomeric bacteriochlorophyll, bacteriopheophytin, and ubiquinones, respectively. Redox midpoint potentials are indicated vs NHE. **B**. The structure of protein estimated by crystallographic analysis (reconstruction from 1PCR file in Protein Data Bank). H-subunit is at the top of the image. The primary donor (P) is at the bottom. The pigments inside the protein scaffold are shown with balls.

Illumination of the constructed RC-functionalized electrodes in buffered solutions led to the generation of photocurrent (Fig. 2). Comparison of the photocurrent at two protein orientations revealed two fundamental effects. First, within the protein the photocurrent always follows the same direction, from the primary donor to the primary acceptor. That is when the RC is bound to the electrode by its H-subunit side, the photocurrent is anodic, and when the RC is bound to the electrode by its P side, the photocurrent is cathodic (Fig. 2A). Second, RC oriented to the electrode at the P side generates considerably higher photocurrent and reaches a photochemical steady state approximately an order of magnitude faster than when oriented at the H-subunit side (Fig. 2C). Applying a bias voltage to the RC-functionalized electrode demonstrates a rectifying effect (Fig. 2B). When RC is bound by its P side the photocurrent is generated only at potentials more negative than 0.3V versus NHE. The midtoint potential for P/P+ couple has been reported to be between 0.46 and 0.55V versus NHE [16, 17]. This suggests overpotential of ~0.2V is needed to see a significant rate for reduction of P+. When the RC is bound to the electrode by its H-subunit side, the photocurrent is generated at potentials more positive then 0.2V versus NHE (Fig. 2B). Ubiquinone at the Qb site has a midpoint potential for theQH2/Q couple between 0.05 and−0.05V versus NHE [18, 19]. This suggests overpotential of ~0.2V is required to see a significant rate for the oxidation of reduced ubiquinone. Using same overpotential (0.3 V), the growth to steady state photocurrent as a function of time for both orientations of RC is shown in Fig. 2C. The data was fit to a single exponential function, $I = I_s(1-\exp(-kt))$, where I is the measured photocurrent at time, t and I_s is the photocurrentat steady state and is the apparent rate constant. For P side, $k=5\pm1$ s^{-1} and for the H-subunit side $k = 0.5\pm0.1$ s^{-1}.

At both orientations RC shows a dependence on the incident photon-to-current conversion efficiency (IPCE) with the wavelength of excitation light (action spectrum) similar to the RC absorption spectrum confirming that the photocurrent is generated by RC.
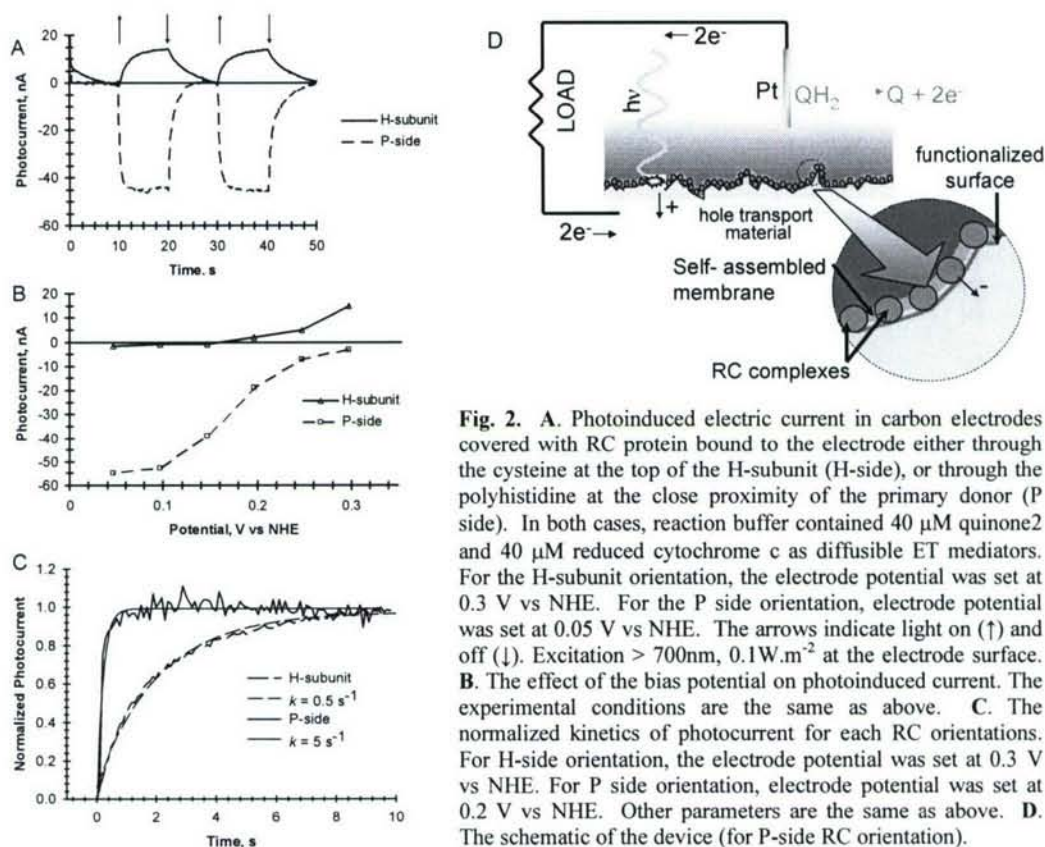
Fig. 2. A. Photoinduced electric current in carbon electrodes covered with RC protein bound to the electrode either through the cysteine at the top of the H-subunit (H-side), or through the polyhistidine at the close proximity of the primary donor (P side). In both cases, reaction buffer contained 40 μM quinone2 and 40 μM reduced cytochrome c as diffusible ET mediators. For the H-subunit orientation, the electrode potential was set at 0.3 V vs NHE. For the P side orientation, electrode potential was set at 0.05 V vs NHE. The arrows indicate light on (↑) and off (↓). Excitation > 700nm, $0.1 W.m^{-2}$ at the electrode surface. **B.** The effect of the bias potential on photoinduced current. The experimental conditions are the same as above. **C.** The normalized kinetics of photocurrent for each RC orientations. For H-side orientation, the electrode potential was set at 0.3 V vs NHE. For P side orientation, electrode potential was set at 0.2 V vs NHE. Other parameters are the same as above. **D.** The schematic of the device (for P-side RC orientation).

The origin of lower efficiency of electron transfer between RC and electrode when the protein facing the surface by its Q-side in not very clear at the moment. To test the effect of electrode coverage for two RC orientations we performed electron microscopic (TEM) examination of carbon electrodes (at high protein concentration) and atomic force microscopic (AFM) examination of gold surfaces (at low protein concentration, so that single protein molecules can be seen). In AFM images, we observed 7-8 nm particles on the surface of the electrodes that are closed to size of RC protein estimated by crystallographic analysis [20]. The average particle densities observed in TEM images (Fig. 3) were approximately 0.017 ± 0.004 per nm^2 for the RC bound at the P side and 0.0150 ± 0.003 per nm^2 for the RC bound at the H-subunit side indicating the similar and high level of coverage for the electrode surfaces in both cases.

We observed no specific protein–protein association or patterning for both protein orientations although linear protein chains and clusters were occasionally seen. When we assume that RC has an average molecular size of ~7 nm then at a 100% surface coverage the density of RC should be approximately 0.02 per nm^2. These results indicate that for our film preparations with both protein orientations we got 75-80% of electrode coverage with the protein. Thus, the decrease in the efficiency of photocurrent in the case of RC facing the electrode with its Q-side is more likely due to the longer distance of electron tunneling between RC internal ET components and the electrode, but not the difference in electrode coverage at two protein orientations. Indeed, according to Marcus' theory, the difference in 1-2 nm (due to the presence H-subunit at protein binding by Q-side) can decrease the efficiency of electron tunneling by several orders of magnitude [21]. (The actual difference in the rate of ET observed in experiments might be less dramatic due to the effects of media, tilting, etc.) Thus, the slower rate to reach the photochemical steady state (and lower photocurrent) for RC bound by its H-subunit side might be due to the increase in the distance between the ET molecules and the electrodes due to insulating effect of H subunit.

These results demonstrate that RC-covered gold and carbon electrodes that we constructed are highly (nearly totally) covered with RC protein. The constructed electrodes can generate photocurrent that direction dramatically depends on protein orientation and thus operate as a photorectifier. The results also show that some parts of RC protein may act as insulators and thus protein modification is required for improving the electrical contact between RC and the electrode.

2. THE EFFECT OF DISTANCE AND DRIVING FORCE ON PHOTO-INDUCED ELECTRIC CURRENT BETWEEN PHOTOSYNTHETIC PROTEIN AND ELECTRODE

For designing efficient electrical contacts between RC and electrode we performed a series of experiments identifying factors controlling ET between immobilized RC and electrodes. We constructed a set of gold electrodes with Ni(NTA)-terminated alkanethiol self-assembled monolayers (SAMs) of different thicknesses (3, 6, 10, and 15 methylene units) and immobilize the RC on top of them through polyHis tag located at the C-terminal end of the protein M-subunit. As we have mention above, this binding allows for specific uniform protein orientation in all our preparation.

The thicknesses of the constructed monolayers were estimated by ellipsometry assuming a 30° tilt for the alkane chain [22-24]. The results demonstrated excellent correlation between predicted and observed thicknesses, linear dependence of the monolayer thickness on the number methylene units within the alkanethiol used, and confirmed nearly 100% of surface coverage with this SAMs for all constructed surfaces (Fig. 3A, Table 1). After conversion of the carboxyl-terminated SAMs to Ni(NTA)-terminated SAMs the thicknesses increased by 3-6 Å which is consistent with a recent report about the thickness of the Ni(NTA) group [25] and indicates moderate disordering introduced by this head-group. After the immobilization of RC on the top of the linkers, the thicknesses of the monolayers increase further by 3-3.4 nm, the same value for all constructed surfaces. (Fig. 3, Table 1).

2.1 Distance attenuation factor.

Illumination of all constructed surfaces led to the generation of electric currents in the supporting electrodes. Fig. 4 depicts the kinetics of photocurrent at the onset of illumination at bias voltage +0.10 V (vs NHE) for the set of the constructed electrodes. As one might expect, the steady-state photocurrent and the rate of achieving it increase dramatically with the decrease in the distances between RC and electrode.

When we plotted the logarithms of steady state "ON" and "OFF" photocurrents vs. distance to electrode we observe two functional areas (Fig. 4B). At short distances to electrode (<1 nm) the current is nearly independent on the distance, but it substantially decreases at distances longer than 1 nm. According to Marcus and others, the rate of electron tunneling between a protein and an electrode should exponentially depend on the distance between RC and electrode [21, 26-28]:

$$k = k_o \exp[-\beta n]$$

where k is the steady state rate of ET for given applied voltage at given SAM thickness (k_o is the rate at zero distance), β is the distance dependence parameter (tunneling attenuation factor), and n is the distance between the protein and electrode expressed in the number of methylene units in the linker. Analysis of the decay of ET with the distance to electrode for the linkers with 10 and 15 methylene units gives distance dependence factor for the constructed surfaces ~ 0.87 per methylene unit (Table 1). That value is typical for alkanethiol SAMs [28-31]. Extrapolation of this dependence to the zero distance allows for estimation of maximal rate constant for electron tunneling between the electrode and RC for the constructed surfaces (k_o=104-105 s^{-1}).

The origin of the factors that can eliminate the rate of ET for immobilized RC at shorter distances to electrode is not clear at the moment. Among them might be charge transfer within the protein and between the protein and the other electrodes, the effects which are not well understood.

2.2 Reorganization energy.
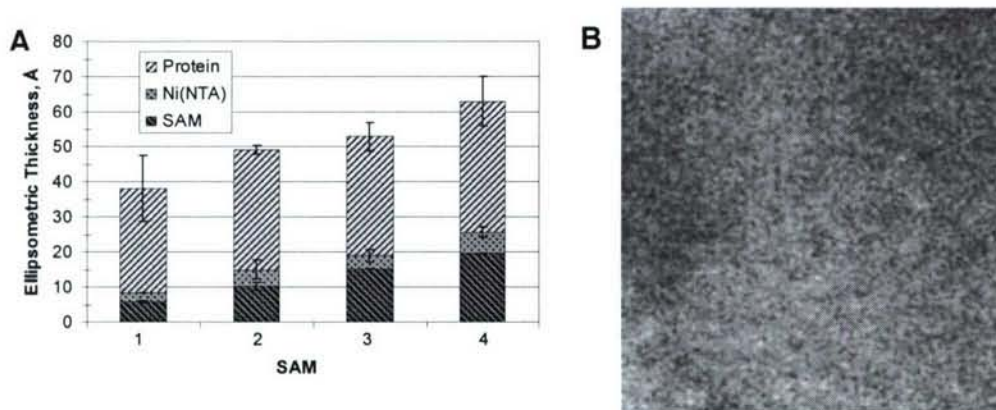
Fig. 3. **A.** Ellipsometric thicknesses of carboxyl terminated (the bottom part of the bars), Ni(NTA) terminal (the bottom + the middle parts of the bars), and RC terminated (the total bars) monolayers made with linkers 1, 2, 3, and 4 on gold electrode. Note the same thickness of the protein layer (the top part of the bars) in all preparations, only the distance to electrode (the bottom parts of the bars) varies. **B.** Electron micrograph of a carbon electrode (carbon grid) covered with RC monolayer (magnification 320 000x).
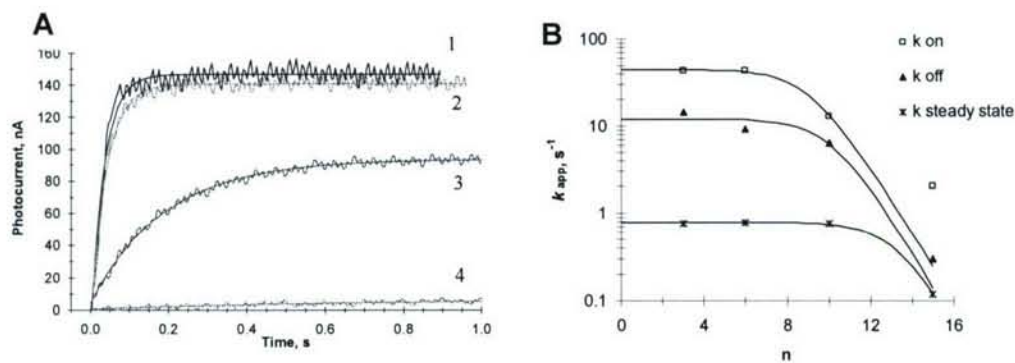

Fig. 4. **A.** Photocurrent transitions at the beginning of illumination for RC-modified gold electrodes with RC proteins sitting on the top of NTA-terminated SAMs made with linkers 1, 2, 3 and 4, respectively. Electrode potential was +0.10 V, other experimental conditions are the same as in figure 2. **B.** Dependence of the rate constant for the photocurrent increase at the beginning of illumination (light ON, □), photocurrent decay at the cessation of illumination (light OFF, ▲), and steady-state photocurrent (*) on the distance between RC and gold electrode (for linkers 1, 2, 3, and 4, expressed at abscissa of the graph in methylene units (n). The fitted lines represent a calculation using $\dfrac{1}{k_{app}} = \dfrac{1}{k_{lim}} + \dfrac{1}{k_o} \exp^{-n\beta}$ with $\beta = 0.87$.

The advantage of photosynthetic RC compare to other photoactive proteins for the construction of photoactive surfaces is in its rather rigid structure that allowing for operation in frozen solutions [2, 6, 32] and in solid-state devices [33]. To estimate reorganization energy of ET between RC and gold electrode we measured ON, OFF and steady-state ET rates for the constructed surfaces at various potentials of the working electrode. Calculations were performed by fitting Marcus' model integrated over the density of electronic states of gold electrode [34, 35] into the experimental data assuming the normal midpoint potential of the primary donor (Em) equal to +0.47 V. The pertinent equations were the following:

$i_{ss,\eta,d} = nFA\, k_{ss,\eta,n}\, \Gamma RC^*$

$k_{ss,\eta,d} = k_{ox,\eta,d} - k_{red,\eta,d}$

$$\eta = E_{app} - E_{mp}$$

$$k_{red,\eta,d} = \mu\rho k_B T \sum_{x=-100}^{100} \left[\frac{\exp\{-(x-(\lambda+\eta)/k_B T)^2 (k_B T/4\lambda)\}}{1+\exp(x)} \right]$$

$$k_{ox,\eta,d} = \mu\rho k_B T \sum_{x=-100}^{100} \left[\frac{\exp\{-(x-(\lambda-\eta)/k_B T)^2 (k_B T/4\lambda)\}}{1+\exp(x)} \right]$$

$$\mu = \mu_o \exp(-\beta d)$$

where $i_{ss,\eta,d}$ is the steady state photocurrent for a given overpotential (η) and SAM thickness (d), n is the number of electrons transferred per RC per reaction event (n = 1), F the Faraday constant (F = 96,487 C/mole e-), A is the electrode area (A = 1 cm^2), Γ_{RC^*} is the surface density of RC (3 x 10^{-13} moles/cm^2) contributing to steady state photocurrent, E_{app} is the potential applied to the electrode, E_{mp} is the midpoint (formal potential) of the cofactor (i.e., cytochrome c or the primary donor) directly exchanging electrons with the electrode, $k_{ss,\eta,n}$ is the η and d dependent net rate of electron transfer from Q2 in solution to the electrode via RC mediated electron-transfer, $k_{ox,\eta,d}$ is the η and d dependent rate of electron transfer from Q2 to the electrode via RC mediated electron-transfer contributing to $k_{ss,\eta,n}$, $k_{red,\eta,d}$ is the η and d dependent rate of electron transfer from the electrode to Q2 via RC mediated electron-transfer contributing to $k_{ss,\eta,n}$, λ is the electron transfer reorganization energy barrier, μ is the distance dependent overlap or coupling between the electronic orbitals of the electrode and cofactor directly exchanging electrons with the electrode, ρ is the density of electronic states of the electrode, μ_o is the orbital coupling at zero distance separating the cofactor and electrode and x is electron energy relative to the Fermi level. T is the temperature and k_B is the Boltzmann constant. It is important to note here that the observed photocurrent was cathodic (i.e. $i_{ss,\eta,d}$ and $k_{ss,\eta,n}$ are < 0) indicating a net transfer of electrons from the electrode.

For the estimation of reorganization energy (λ) from experimental data, we approximate the ET rate constant k_η by the discrete sums as described above and then minimize the deviation of the rate constants $k_\eta(\lambda)$ as a function of λ from the measured rate constants $\bar{k}_\eta$:

$$\min_\lambda \sum_\eta (k_\eta(\lambda) - \bar{k}_\eta)^2$$

Minimization was done by Newton's method using modified software LOQO [36].

For the short linkers our calculations show consistent low reorganization energy (λ = 0.21-0.23 eV for ON, OFF and steady-state photocurrent (Table 2). This low λ is similar to estimated for ET within the protein in solution by differential absorption spectroscopy [21, 26-28] and confirms the idea that protein-short linker-electrode complexes have rigid structures and do not perform substantial conformational changes in the course of photoactivation. At longer distance between RC and electrode the results show considerable increase in λ (Table 2) possibly due to linker mobility and protein tilting.

Thus, after immobilization, photosynthetic RC retains its shape and the main ET properties, including its ability for photoinduced ET, similar to those estimated for this protein by differential absorption spectroscopy in solution and *in vivo*. The ET between RC and electrodes occurs with low reorganization energy (0.23 eV) and thus the surfaces are suitable for the construction of solid-state photoelectronic and photovoltaic devices. The ET in the constructed monolayers follows tunneling mechanism with distance dependence factor equal to 0.87 per methylene unit. Estimated by extrapolation from nonadiabatic area the maximal tunneling rate constant for ET from the flat electrode to RC primary donor is about 10^5-10^6 s^{-1}, and thus, additional protein and electrode modifications might be required for improving electrical contact between the protein and electrode.

Table 1. Thicknesses (in Å) of gold electrodes with carboxy-terminated SAMs, Ni(NTA)-terminated SAMs, and Ni(NTA)-terminated SAMs with bound poly histidine-labeled RCs. Thickness of the protein layers was calculated by subtraction of thickness of underlying Ni(NTA)-terminated SAMs.

Linker name	Linker length (methylene units)	Carboxy-terminated SAM by ellipsometry (Å)	Carboxy-terminated SAM by model (Å)	Ni(NTA)-terminated SAM by ellipsometry (Å)	RC-terminated SAM by ellipsometry (Å)	RC layer thickness by ellipsometry (Å)
1	3	5.9 ± 0.3	5.6	8.4 ± 1	38.4 ± 9	30
2	6	10.3 ± 1	8.8	15.0 ± 2.8	49.0 ± 1.4	34
3	10	15.1 ± 0.1	13.2	18.9 ± 1.7	52.9 ± 4	34
4	15	19.6 ± 0.1	18.8	25.6 ± 1.5	63.3 ± 7	37

Table 2. Transition rates (k, in s^{-1}) and RC reorganization energies (λ, eV) estimated from the transient kinetics of photocurrent between RC and gold electrode at onset of illumination (ON), at cessation of illumination (OFF) (k_{on}, k_{off}, in s^{-1}, respectively) and from the steady-state photocurrent (Iss, in nA/cm^2) at various electrode potentials (in V vs NHE) and linker lengths (L, in methylene units) assuming normal midpoint potential of the special pair = +0.47 V vs NHE.

Electrode Potential (V vs NHE)	L=3 methylene units			L=6 methylene units			L=10 methylene units			L=15 methylene units		
	$k_{on}(s^{-1})$	$k_{off}(s^{-1})$	Iss (nA/cm^2)	$k_{on}(s^{-1})$	$k_{off}(s^{-1})$	Iss (nA/cm^2)	$k_{on}(s^{-1})$	$k_{off}(s^{-1})$	Iss (nA/cm^2)	$k_{on}(s^{-1})$	$k_{off}(s^{-1})$	Iss (nA/cm^2)
0	43	14.4	161	43	9.1	167	13	6.3	158.5	2	0.3	25.3
0.05	42	12.3	148	34	9.6	133	8.6	3.7	114	1.8	0.08	11.7
0.1	41	11.7	129	31.6	8.2	94	7.5	1.9	82	1.5	-	5.3
0.15	40.5	7.4	109	21.9	6.6	74	4	1	48.5	-	-	2
0.2	28	4.5	68	17.2	4.8	43	3	0.59	26.5	-	-	0.5
0.25	8	-	25	15.8	3.1	14.5	-	0.38	10	-	-	0
λ (eV)	**0.21**	**0.23**	**0.23**	**0.21**	**0.21**	**0.25**	**0.23**	**0.25**	**0.28**	n/a	n/a	**0.64**
Error (%)	14	4.7	0.18	11.7	2.9	0.15	3.5	1.2	0.12	n/a	n/a	0.01

3. CONSTRUCTION OF SOLID-STATE PHOTOVOLTAIC DEVICES BASED ON PHOTOSYNTHETIC PROTEINS

The principles developed in our work with RC-functionalized electrodes in buffered solutions formed a background for the construction of an RC-based solid-state photovoltaic device. In this case instead of buffer we used ITO and C60 as conductive materials [33].

The short circuit current density of the constructed photovoltaic device was 0.12 mA/cm^2 under an excitation intensity of 10W/cm^2 at λ=808 nm. Assuming a perfectly formed RC monolayer of density 3 x 10^{-12} mol.cm^2, and given an extinction coefficient of 2.9 x 10^5 M^{-1} cm^{-1}, [37] we calculate the optimum photocurrent as 1 mA/cm^2, where we have ignored possible micro cavity effects due to reflections from the ITO/Au electrode and assumed 100% reflection of the optical pump by the Ag cathode. Thus, under short-circuit conditions, a conservative estimate of the internal quantum efficiency of the device is 12%. These results suggest that photosynthetic complexes may be used as an interfacial material in photovoltaic devices. Evolved within a thin membrane interface, photosynthetic complexes sustain large open circuit voltages of 1.1V [6] without significant electron-hole recombination, and they may be self-assembled into an insulating membrane, further reducing recombination losses. Given typical quantum yields for photo-induced charge generationı of >95% it is expected that the power conversion efficiency of a RC-based solid-state photovoltaic device may approach or exceed 20%. [33]

4. FABRICATION OF SELF-ASSEMBLED PROTEIN SUPRACOMPLEXES ON INORGANIC ELECTRODES

In photosynthesis, cytochrome c acts as a diffusible ET mediator to the RC primary donor. Precisely adapted by the evolution for the interaction with RC, cytochrome c penetrates inside the RC protein at the side of primary donor (special pair, P) leading to a high efficiency of ET between these two proteins [38-41]. At the same time, because of a relatively small size cytochrome can efficiently exchange electrons with electrodes at either protein orientation after immobilization on electrode surface [30, 42-44]. Therefore, if a RC-cytochrome complex can be formed on an electrode it might open a possibility for an efficient electrical connection between RC and the electrode.

To test the possibility for the construction of a multi-protein ET chain (a supracomplex of RC and a cytochrome) on an electrode, we initially assembled a SAM with oriented and aligned monolayers of RC protein on gold electrodes [4]. The carboxyl terminated alkanethiol self-assembled monolayer was formed as described above and then converted to nitrillotriacetic acid (NTA) terminated SAM. After chelating this surface with Ni^{2+}, an oriented RC layer with the primary donor facing the electrode was assembled on the top of the SAM layer [4]. Then cytochrome c (horse heart, Sigma) was added to the buffer and incubated with the electrode for about an hour [45].

Illumination of the constructed surface demonstrated its ability to generate photocurrent with the direction of electron transfer from the electrode to protein and thus confirmed the expected protein orientation. After incubation with cytochrome c we observed a time-dependent improvement of the photocurrent which after few minutes of incubation reached an intensity of 40-100 times higher than the initial value (Fig. 5). The increase in photocurrent was observed both with oxidized and reduced forms of cytochrome c. Washing out the cytochrome after the photocurrent reached saturation (about 1 min of incubation with cytochrome c) did not reduce it to the initial low level, indicating the irreversible nature of the changes induced by cytochrome in the system.

To test the possibility of the formation of a complex between the proteins on electrode we performed surface plasmon resonance (SPR) experiments (with Biacore 3000, Sweden). In these experiments commercial NTA-chips (Biacore) were used. In the course of the experiments the NTA surface was initially activated with NiCl$_2$ and then RC protein was added. The extent of both Ni^{2+} and RC binding to the surface were followed by SPR (Fig. 5). After RC binding to the chip and removing of excess RC protein with running buffer, cytochrome c was injected into the buffer and the increase in the surface thickness was monitored. The efficiency of bindings (i.e., the binding and dissociation constants) of RC to Ni-NTA and

cytochrome c to RC were calculated from the experimental curves obtained at various concentrations of the proteins. The results were compared to the know for the proteins in lipid layers and in solutions (Table 3). The data demonstrate RC-cytochrome dissociation constants K_D = 0.8e-8 and 11e-8 (M) for reduced and oxidized forms of cytochrome, respectively. That is similar to the estimated binding constants of the same forms of cytochrome to RC imbedded in lipid membrane (K_D = 1.0e-8 and 15e-8 (M)) [46], and for interaction of cytochrome and RC proteins in solution (K_D = 30e-8 (M)) measured by spectroscopic techniques [41].
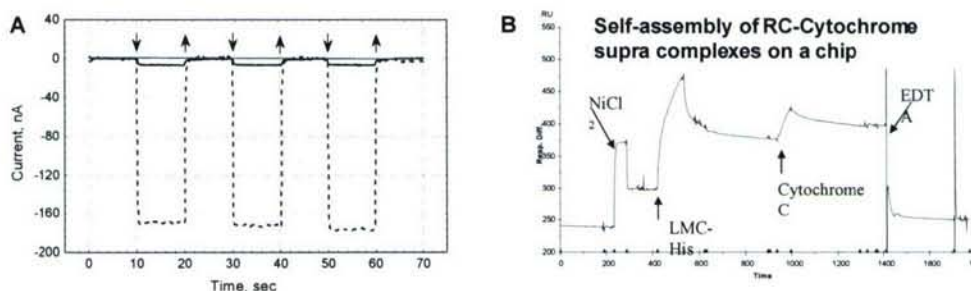
Fig. 5. A. Steady state photocurrent in gold electrode covered with RC and with (– – –) and without (———) cytochrome c. The arrows indicate light ON (↓) and OFF (↑). B. SPR detection of the binding of Ni2+, RC, and cytochrome to NTA surface. The arrows indicate the periods of time ON (↑) and OFF (↓) when NiSO4, RC, cytochrome c, and EDTA were in the running buffer.

Estimation of the ratio between RC and cytochrome in the constructed complexes from the intensity of SPR signals belonging to RC and cytochrome after a correction for their molecular masses (96 and 13 kD, respectively [11, 46, 47]) gives ratio 1:1.04 (Fig. 5) indicating the formation of 1:1 complexes between these two proteins. The addition of 0.35 M EDTA, a chelator that specifically disrupts the NTA-Ni-polyHis complex, to the running buffer removes most of the proteins from the surface conferring specific binding of RC-cytochrome complex to the electrode through RC polyhistidine tag.

Table 3. Kinetic parameters for the binding of cytochrome c to RC on electrode surfaces.

Reaction	Ka (1/Ms)	Kd (1/s)	K_D (M)	Surface	Reference
Oxidized Cyt to RC-WT	95.5e3	4.71e-3	4.93e-8	COOH	This work
Oxidized Cyt to RC-his	2.64e3	2.19e-3	0.83e-8	Ni-NTA	This work
Reduced Cyt to RC-his	9.71e3	1.07e-3	11e-8	Ni-NTA	This work
Oxidized Cyt c to RC-WT			1.0e-8	Lipid Layer	[46]
Reduced Cyt c to RC-WT			15.0e-8	Lipid Layer	[46]
Reduced(?)Cyt to RC-WT			30e-8	Solution	[41]

where Ka is association constant, Kd is dissociation constant, and K_D is binding constant.

These results show that the wiring of RC special pair that is deeply buried inside the protein to the electrode can be substantially improved by incorporation into RC-SAM-electrode complex another protein, cytochrome c. The same principles of self-assembly protein supracomplexes on a chip can be utilized for the construction of other highly efficient photovoltaic and photo-electronic devices.

5. CONCLUSIONS

Our results demonstrate that being bound to inorganic electrodes photosynthetic reaction centers can serve as efficient photovoltaic devices, optical switches, or rectifiers. For ET between RC and electrode a design with direct tunneling might be the best choice. Biological principles of protein self-assembly seem to be efficient for the construction of multifunctional supramolecular ET complexes.

27

6. PUBLICATIONS (2006)

1. Trammell, S.A., Spano, A., Price, R., Lebedev, N.: Effect of protein orientation on electron transfer between photosynthetic reaction centers and carbon electrode. - **Biosensors & Bioelectronics**, 21:1023-1028, 2006
2. Carissa M. Soto, Amy Szuchmacher Blum, Gary J. Vora, Nikolai Lebedev, Carolyn E. Meador, Angela P. Won1, Anju Chatterji, John E. Johnson, and Banahalli R. Ratna: Fluorescent signal amplification of carbocyanine dyes using engineered viral nanoparticles. - **JACS** 128:5184-5189, 2006
3. Nikolai Lebedev, Scott A. Trammel, Anthony Spano, Evgeny Lukashev, Igor Griva and Joel Schnur: Conductive wiring of immobilized photosynthetic Reaction Center to electrode by Cytochrome c. **JACS** 128:12044-12045, 2006
4. Scott A. Trammell, Dwight S. Seferos, Martin Moore, Daniel A. Lowy, Guillermo C. Bazan, James G. Kushmerick, and Nikolai Lebedev: Proton-Coupled Electron-Transfer Mediated by Oligo(phenylene vinylene) Bridges. - **Langmuir** 23:942-948, 2007

ACKNOWLEDGEMENTS

REFERENCES

1. Gratzel, M., *Photoelectrochemical cells.* Nature, 2001. **414**(6861): p. 338-344.
2. Sundstrom, V., *Light in elementary biological reactions.* Progress in Quantum Electronics, 2000. **24**(5): p. 187-238.
3. Feher, G., et al., *Structure and Function of Bacterial Photosynthetic Reaction Centers.* Nature, 1989. **339**(6220): p. 111-116.
4. Trammell, S.A., et al., *Orientated binding of photosynthetic reaction centers on gold using Ni-NTA self-assembled monolayers.* Biosensors & Bioelectronics, 2004. **19**(12): p. 1649-1655.
5. Lee, I., et al., *Measurement of electrostatic potentials above oriented single photosynthetic reaction centers.* Journal of Physical Chemistry B, 2000. **104**(11): p. 2439-2443.
6. Hoff, A.J. and J. Deisenhofer, *Photophysics of photosynthesis. Structure and spectroscopy of reaction centers of purple bacteria.* Physics Reports-Review Section of Physics Letters, 1997. **287**(1-2): p. 2-247.
7. King, B.A., et al., *Excited-state energy transfer pathways in photosynthetic reaction centers: 5. Oxidized and triplet excited special pairs as energy acceptors.* Chemical Physics, 2003. **294**(3): p. 359-369.
8. Yakovlev, A.G., et al., *Mechanism of charge separation and stabilization of separated charges in reaction centers of Chloroflexus aurantiacus and of YM210W(L) mutants of Rhodobacter sphaeroides excited by 20 fs pulses at 90 K.* Journal of Physical Chemistry A, 2003. **107**(40): p. 8330-8338.
9. Zhao, J.Q., et al., *Differentiating the orientations of photosynthetic reaction centers on Au electrodes linked by different bifunctional reagents.* Biosensors & Bioelectronics, 2002. **17**(8): p. 711-718.
10. Trammell, S.A., et al., *Effect of protein orientation on electron transfer between photosynthetic reaction centers and carbon electrodes.* Biosensors & Bioelectronics, 2006. **21**(7): p. 1023-1028.
11. Goldsmith, J.O. and S.G. Boxer, *Rapid isolation of bacterial photosynthetic reaction centers with an engineered poly-histidine tag.* Biochimica Et Biophysica Acta-Bioenergetics, 1996. **1276**(3): p. 171-175.
12. Rosenow, M.A., et al., *The influence of detergents on the solubility of membrane proteins.* Acta Crystallographica Section D-Biological Crystallography, 2002. **58**: p. 2076-2081.

13. Katz, E., *Application of Bifunctional Reagents for Immobilization of Proteins on a Carbon Electrode Surface - Oriented Immobilization of Photosynthetic Reaction Centers*. Journal of Electroanalytical Chemistry, 1994. **365**(1-2): p. 157-164.

14. Che, G.L., et al., *Carbon nanotubule membranes for electrochemical energy storage and production*. Nature, 1998. **393**(6683): p. 346-349.

15. Li, J., et al., *Highly-ordered carbon nanotube arrays for electronics applications*. Applied Physics Letters, 1999. **75**(3): p. 367-369.

16. Ivancich, A., et al., *Effects of hydrogen bonds on the redox potential and electronic structure of the bacterial primary electron donor*. Biochemistry, 1998. **37**(34): p. 11812-11820.

17. Moss, D.A., et al., *Electrochemical Redox Titration of Cofactors in the Reaction Center from Rhodobacter-Sphaeroides*. Febs Letters, 1991. **283**(1): p. 33-36.

18. Crofts, A.R. and C.A. Wraight, *The Electrochemical Domain of Photosynthesis*. Biochimica Et Biophysica Acta, 1983. **726**(3): p. 149-185.

19. Rutherford, A.W. and M.C.W. Evans, *Direct Measurement of the Redox Potential of the Primary and Secondary Quinone Electron-Acceptors in Rhodopseudomonas-Sphaeroides (Wild-Type) by Electron-Paramagnetic-Res Spectrometry*. Febs Letters, 1980. **110**(2): p. 257-261.

20. Allen, J.P., et al., *Structure of the Reaction Center from Rhodobacter-Sphaeroides R-26 - the Protein Subunits*. Proceedings of the National Academy of Sciences of the United States of America, 1987. **84**(17): p. 6162-6166.

21. Marcus, R.A. and N. Sutin, *Electron Transfers in Chemistry and Biology*. Biochimica Et Biophysica Acta, 1985. **811**(3): p. 265-322.

22. Ferretti, S., et al., *Self-assembled monolayers: a versatile tool for the formulation of bio-surfaces*. Trac-Trends in Analytical Chemistry, 2000. **19**(9): p. 530-540.

23. Flink, S., F. van Veggel, and D.N. Reinhoudt, *Sensor functionalities in self-assembled monolayers*. Advanced Materials, 2000. **12**(18): p. 1315-1328.

24. Sigal, G.B., et al., *A self-assembled monolayer for the binding and study of histidine tagged proteins by surface plasmon resonance*. Analytical Chemistry, 1996. **68**(3): p. 490-497.

25. Lee, J.K., et al., *Grafting nitrilotriacetic groups onto carboxylic acid-terminated self-assembled monolayers on gold surfaces for immobilization of histidine-tagged proteins*. Journal of Physical Chemistry B, 2004. **108**(23): p. 7665-7673.

26. Arnaut, L.G. and S.J. Formosinho, *Theory of electron transfer reactions in photosynthetic bacteria reaction centers*. Journal of Photochemistry and Photobiology a-Chemistry, 1997. **111**(1-3): p. 111-138.

27. Beratan, D.N., J.N. Betts, and J.N. Onuchic, *Tunneling Pathway and Redox-State-Dependent Electronic Couplings at Nearly Fixed Distance in Electron-Transfer Proteins*. Journal of Physical Chemistry, 1992. **96**(7): p. 2852-2855.

28. Page, C.C., et al., *Natural engineering principles of electron tunnelling in biological oxidation-reduction*. Nature, 1999. **402**(6757): p. 47-52.

29. Jeuken, L.J.C., et al., *Electron-transfer mechanisms through biological redox chains in multicenter enzymes*. Journal of the American Chemical Society, 2002. **124**(20): p. 5702-5713.

30. Khoshtariya, D.E., et al., *Charge-transfer mechanism for cytochrome c adsorbed on nanometer thick films. Distinguishing frictional control from conformational gating*. Journal of the American Chemical Society, 2003. **125**(25): p. 7704-7714.

31. Murgida, D.H. and P. Hildebrandt, *Electron-transfer processes of cytochrome c at interfaces. New insights by surface-enhanced resonance Raman spectroscopy*. Accounts of Chemical Research, 2004. **37**(11): p. 854-861.

32. Kleinfeld, D., M.Y. Okamura, and G. Feher, *Electron-Transfer Kinetics in Photosynthetic Reaction Centers Cooled to Cryogenic Temperatures in the Charge-Separated State - Evidence for Light-Induced Structural-Changes*. Biochemistry, 1984. **23**(24): p. 5780-5786.

33. Das, R., et al., *Integration of photosynthetic protein molecular complexes in solid-state electronic devices*. Nano Letters, 2004. **4**(6): p. 1079-1083.

34. Chidsey, C.E.D., *Free-Energy and Temperature-Dependence of Electron-Transfer at the Metal-Electrolyte Interface*. Science, 1991. **251**(4996): p. 919-922.

35. Tender, L., M.T. Carter, and R.W. Murray, *Cyclic Voltammetric Analysis of Ferrocene Alkanethiol Monolayer Electrode-Kinetics Based on Marcus Theory*. Analytical Chemistry, 1994. **66**(19): p. 3173-3181.

36. Griva, I., *Numerical experiments with an interior-exterior point method for nonlinear programming.* Computational Optimization and Applications, 2004. **29**(2): p. 173-195.

37. Straley, S.C., et al., *Pigment Content and Molar Extinction Coefficients of Photochemical Reaction Centers from Rhodopseudomonas-Spheroides.* Biochimica Et Biophysica Acta, 1973. **305**(3): p. 597-609.

38. Axelrod, H.L. and M.Y. Okamura, *The structure and function of the cytochrome c(2): reaction center electron transfer complex from Rhodobacter sphaeroides.* Photosynthesis Research, 2005. **85**(1): p. 101-114.

39. Lin, X., et al., *Relationship between Rate and Free-Energy Difference for Electron-Transfer from Cytochrome C(2) to the Reaction-Center in Rhodobacter-Sphaeroides.* Biochemistry, 1994. **33**(46): p. 13517-13523.

40. Miyashita, O., J.N. Onuchic, and M.Y. Okamura, *Transition state and encounter complex for fast association of cytochrome c(2) with bacterial reaction center.* Proceedings of the National Academy of Sciences of the United States of America, 2004. **101**(46): p. 16174-16179.

41. Paddock, M.L., et al., *Interactions between cytochrome c(2) and the photosynthetic reaction center from Rhodobacter sphaeroides: The cation-pi interaction.* Biochemistry, 2005. **44**(28): p. 9619-9625.

42. Haas, A.S., et al., *Cytochrome c and cytochrome c oxidase: Monolayer assemblies and catalysis.* Journal of Physical Chemistry B, 2001. **105**(45): p. 11351-11362.

43. Heering, H.A., et al., *Direct immobilization of native yeast Iso-1 cytochrome c on bare gold: Fast electron relay to redox enzymes and zeptomole protein-film voltammetry.* Journal of the American Chemical Society, 2004. **126**(35): p. 11103-11112.

44. Murgida, D.H. and P. Hildebrandt, *Redox and redox-coupled processes of heme proteins and enzymes at electrochemical interfaces.* Physical Chemistry Chemical Physics, 2005. **7**(22): p. 3773-3784.

45. Vanderkooi, J.M., F. Adar, and M. Erecinska, *Metallocytochromes-C - Characterization of Electronic Absorption and Emission-Spectra of Sn-4+ and Zn-2+ Cytochromes-C.* European Journal of Biochemistry, 1976. **64**(2): p. 381-387.

46. Miyashita, O., M.Y. Okamura, and J.N. Onuchic, *Theoretical understanding of the interprotein electron transfer between cytochrome c(2) and the photosynthetic reaction center.* Journal of Physical Chemistry B, 2003. **107**(5): p. 1230-1241.

47. Gray, H.B. and J.R. Winkler, *Electron tunneling through proteins.* Quarterly Reviews of Biophysics, 2003. **36**(3): p. 341-372.